

## Delocalization of Nonlinear Optical Responses in Plasmonic Nanoantennas

Sviatlana Viarbitskaya,<sup>\*</sup> Olivier Demichel, Benoît Cluzel, Gérard Colas des Francs, and Alexandre Bouhelier<sup>†</sup>  
*Laboratoire Interdisciplinaire Carnot de Bourgogne CNRS-UMR 6303, Université Bourgogne Franche-Comté, 21078 Dijon, France*

(Received 26 March 2015; published 4 November 2015)

Remote excitation and emission of two-photon luminescence and second-harmonic generation are observed in micrometer long gold rod optical antennas upon local illumination with a tightly focused near-infrared femtosecond laser beam. We show that these nonlinear radiations are emitted from the entire antenna and the measured far-field angular patterns bear the information regarding the nature and origins of the respective nonlinear processes. We demonstrate that the nonlinear responses are locally induced by a propagating surface plasmon at the excitation frequency, enabling thereby a polariton-mediated spatial tailoring and design of coherent and incoherent nonlinear responses.

DOI: 10.1103/PhysRevLett.115.197401

PACS numbers: 78.67.-n, 42.25.Kb, 42.65.Ky, 78.67.Uh

Optical antennas are pervasive devices controlling the spatial, spectral, and angular distributions of light on subdiffraction length scales [1,2]. This unique asset is enabled by a precise engineering of the underlying surface plasmon (SP) resonances. Facilitated by the enhanced electromagnetic field associated with these polaritonic resonances, optical antennas are rapidly entering a new operating regime whereby nonlinear responses are emerging to improve nanoscale light management [3–5]. A nonlinear optical antenna combines the functionalities of linear devices (extreme light concentration, tailoring of spatial and phase distributions, directivity of emission, etc.) with the benefits of nonlinear optical effects, such as frequency conversion [6,7], ultrafast switching [8], modulation [9,10], and self-action [11,12], to name just a few. Nonlinear processes generated by small nanoparticles are largely governed by the localized SP resonances at the frequency of the driving optical field [4,13–17]. Similarly, for spatially extended plasmonic objects point-and-probe nonlinear scanning microscopy unambiguously revealed the importance of SP modal landscapes [16,18–22]. Hence, designing and controlling the lateral extension of the plasmon mode is a prerequisite for developing advanced nanoscale optical devices as exemplified for nanowire-based coherent light sources [23,24] and strongly coupled systems [25]. In this Letter, we take advantage of a delocalized plasmon distribution to generate spatially extended nonlinear coherent and incoherent sources of photons. To this aim, we discuss two nonlinear optical processes—incoherent two-photon luminescence (TPL) and coherent second-harmonic generation (SHG)—emitted from gold rod optical antennas upon local illumination with a tightly focused femtosecond near-infrared laser beam [16,18–22,26,27]. We demonstrate that nonlinear conversions are not restricted to the excitation area but are spatially delocalized along the entire structure. We argue that the wavelength conversions are mediated by a propagating SP at the excitation frequency despite the associated high losses.

We substantiate this hypothesis by modeling far-field SHG signatures as originating from a nanoscale analog of a phased array antenna [28]. Such an array is composed of coherent dipolar sources oscillating at the SHG frequency, whose amplitudes and phases are determined by the damped SP at the fundamental frequency.

Optical gap antennas are fabricated by electron-beam lithography and lift-off technique on a glass substrate. Each antenna consists of two identical nanowires separated by a gap. The dimensions of individual nanowires are 110 nm in width and 50 nm in height. The length  $L$  of each arm and the gap separation  $g$  are systematically varied from  $300 \text{ nm} < L < 4000 \text{ nm}$ , and from  $0 \text{ nm} < g < 150 \text{ nm}$ , with a minimum gap size of approximately 20 nm, as measured with a scanning electron microscope (SEM). Optical excitation and collection are performed using an inverted microscope. A 180 fs Ti:sapphire laser tuned at a fundamental wavelength of  $\lambda_0 = 810 \text{ nm}$  is focused on the antennas in a diffraction-limited spot by a high numerical aperture objective (oil immersion,  $\text{NA} = 1.49$ ). The laser peak intensity at the sample is  $5 \times 10^{10} \text{ W/cm}^2$ . The incident beam is linearly polarized along the antenna. Nonlinear signals are collected by the same objective followed by a dichroic beam splitter, which separates the useful spectral range (375–700 nm) from the backscattered fundamental beam. Simultaneous confocal maps of spectrally separable TPL and SHG (see the Supplemental Material [29]) are collected by two avalanche photodiodes in the absence of a spatial filter, allowing detection of signal emitted from the entire structure. A 10 nm narrow bandpass filter centered at 405 nm is used for SHG detection. Fourier and direct plane imaging are recorded by separate cameras and relay lenses appropriately placed in their respective conjugate planes [34].

TPL is an incoherent nonlinear optical process defined by the material's electronic band structure [30,35,36] and underlying plasmonic modes [17,18,21,22,37]. In conjunction with the confocal mapping technique, it probes the

local electric field intensity in plasmonic objects [18,38]. SHG point-and-probe mapping provides some additional information about the nonlinear material due to its intrinsic dependency on structural symmetries [19,20,39]. Having detected both signals emitted from lithographic rod antennas, we find that, apart from the difference in the nonlinear yield (see the Supplemental Material [29]), confocal nonlinear maps are practically identical as illustrated in Figs. 1(a) and 1(b). Confocal TPL and SHG mappings are thus ineffective at discerning differences between these two processes. This was true for all studied antennas, regardless of the length or the gap size. Because of this similarity, we rule out any significant structural symmetry-dependent SHG component, which could render the SHG maps to be somewhat different from the TPL ones [4]. It follows that the spatial variations of both SHG and TPL signals must be accounted for by the same sensitivity to the local plasmonic modal distribution [22,40].

While nonlinear confocal mapping fails at distinguishing between these fundamentally different processes, Fourier plane imaging unveils the information hidden in the pixels of the confocal maps. In Figs. 1(d) and 1(e), we compare Fourier plane images representing the projected angular distributions of the TPL and SHG emissions from a single rod antenna [bottom nanowire in Figs. 1(a)–1(c)]. When the laser is focused on the left extremity, the TPL Fourier distribution [Fig. 1(d)] features a pattern with two maxima aligned along the antenna's  $x$  axis coinciding with the excitation polarization direction, at variance with a single  $x$ -oriented dipole [41]. Vastly different is the SHG angular image, shown in Fig. 1(e). It displays distinct interference

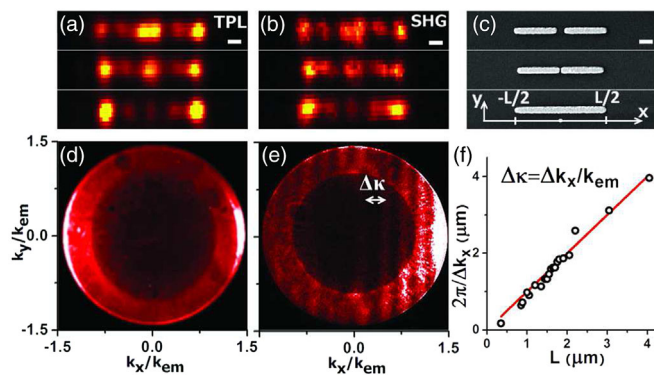


FIG. 1 (color online). (a)–(c) TPL and SHG confocal maps and SEM micrographs of three gold rod antennas. The arm lengths are 650 nm, and the gaps are  $g = 130$  and 50 nm. Scale bars are 200 nm. (d),(e) Angular distributions of TPL and SHG signal from a single nanowire [bottom antenna in (a)–(c)]. The laser is focused at the left extremity. (f) Dependence of  $2\pi/\Delta k_x$  on  $L$  (black  $\circ$ ) and  $2\pi/\Delta k_x = L$  (line). The axes are normalized in units of  $k_{em} = n_m 2\pi/\lambda_{em}$ , where  $\lambda_{em}$  is the emission wavelength of the nonlinear process in vacuum and  $n_m = 1.55$  is the refractive index of glass and oil. The interfringe distance  $\Delta\kappa$  is denoted with the white double-headed arrow.

fringes revealing the coherence of SHG. Excitation at the left antenna extremity systematically produces fringe patterns with an intensity increasing towards positive  $k_x/k_{em}$ . Such a fringe pattern was already observed in a linear regime for bare [42,43] and decorated nanowires [41]. SHG Fourier images show a strict dependence on the rod length. Figure 1(f) displays the reciprocal evolution of the fringe period  $\Delta k_x$  with the antenna length. As TPL is intrinsically an incoherent process, we do not observe interferences in reciprocal space even when a narrow portion of the broad TPL spectrum was spectrally selected (see the Supplemental Material [29]). The TPL Fourier images also do not depend on the antenna's length, and patterns similar to that in Fig. 1(d) are persistently obtained.

SHG Fourier plane imaging of coupled optical gap antenna shows sensitivity to the gap size. Figures 2(a)–2(c) illustrate a set of Fourier planes obtained from three antennas having identical arm lengths (approximately 830 nm) and gaps of 140 nm, 40 nm, and at contact, correspondingly. The excitation is located at their respective right extremities. For maximally decoupled arms [ $g = 140$  nm, Fig. 2(a)], we observe four wide fringes, which, as the gap size decreases, start to split [Fig. 2(b)] and form a pattern of a different symmetry. The splitting becomes more pronounced as the gap decreases to its minimum. A Fourier pattern corresponding to the case of touching arms [Fig. 2(c)] contains a double number of fringes as compared to the case of maximally separated arms. We attribute such splitting or pairing of fringes to the onset of coupling between the antenna's arms.

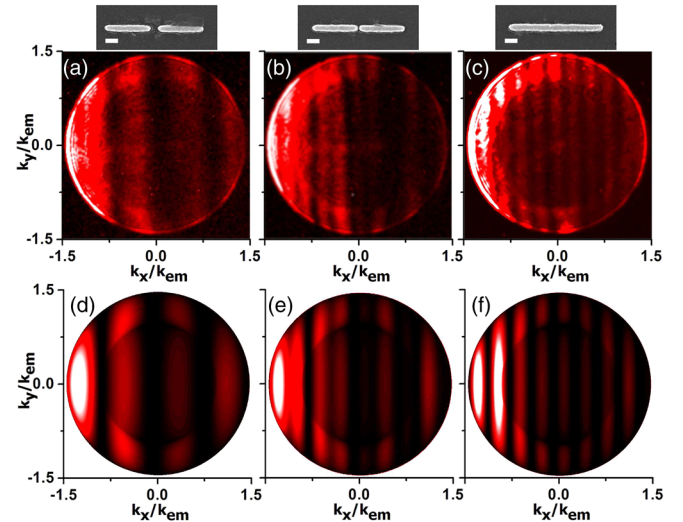


FIG. 2 (color online). (a)–(c) Evolution of experimental Fourier planes with the gap size  $g = 140$ , 40 and 0 nm. The antenna's arm length is 830 nm, and excitation is at the right extremity. Simulated Fourier planes: (d)  $L_{sim} = 720$  nm, (e) far-field beating between  $L_{sim} = 720$  nm and 1700 nm, (f)  $L_{sim} = 1700$  nm. The effective refractive index at  $\lambda_0$  is  $n_{eff} = 1.73$ , and the propagation length is  $L_{sp} = 2100$  nm.

The sensitivity of SHG Fourier planes to the antenna's length and the gap size indicates that the nonlinear response is not simply generated locally by the focused laser beam. To account for the SHG Fourier planes' length dependence, we assume in the following that a surface plasmon excited at  $\lambda_0$  creates an enhanced electric field along the antenna strong enough to distribute the nonlinear optical interactions during its propagation. This assumption is motivated by the fact that a laser beam focused at a nanorod extremity is a prevalent technique used to launch SP in nanowires [31,44,45]. For simplicity, let us consider the propagation of a SP in a one-dimensional cavity (ODC) of length  $L_{\text{sim}}$  [46] mimicking the nanowire. Upon a point dipole excitation at the cavity's left extremity ( $x = -L_{\text{sim}}/2$ ), which we equate here with the focused laser beam excitation, the SP's electric field along the antenna  $E_{\text{SP}}^{\omega}(x)$  can be written as [46]

$$E_{\text{SP}}^{\omega}(x) = E_0 e^{ik_{\text{SP}}L_{\text{sim}}/2} (r + 1) \frac{e^{ik_{\text{SP}}x} - r e^{ik_{\text{SP}}(L_{\text{sim}}-x)}}{1 - r^2 e^{i2k_{\text{SP}}L_{\text{sim}}}}, \quad (1)$$

where  $E_0$  is the excitation field amplitude and  $r$  is the ODC's reflection coefficient. The value of the SP wave vector  $k_{\text{SP}}$  and decay length  $L_{\text{SP}}$  are extracted from finite element simulations [47] of an infinitely long gold nanowire with a  $100 \times 50 \text{ nm}^2$  cross section [48]. Far-field SHG is then phenomenologically modeled by a large number of identical noninteracting dipoles  $p^{2\omega}$  along  $-L_{\text{sim}}/2 \leq x \leq L_{\text{sim}}/2$ , oscillating at the SHG angular frequency. The dipoles are oriented along the antenna's  $y$  axis on the glass-air interface (see the Supplemental Material [29]) and are separated by distance  $d$  with  $d \ll \lambda_{2\omega}$ . The amplitudes and phases of the individual oscillators are position dependent on the ODC scalar plasmon field  $E_{\text{SP}}^{\omega}(x)$ , according to  $p^{2\omega}(x) = \beta^{(2)} [E_{\text{SP}}^{\omega}(x)]^2$ , where  $\beta^{(2)}$  is a 1D counterpart of the nonlinear polarizability of the individual dipoles. Thus, the nonlinearity is modeled via an effective local surface term [26,27]. Note that in our case the interband structure of gold inhibits plasmon modes at the SHG frequency due to absorption. This prevents tailoring of plasmonic modes at the frequency of the nonlinear response, in contrast to recent SHG study [49] and to nanowire-based plasmon lasers [23,24].

Far-field Green functions were used to calculate the coherent sum of electric fields from the SHG dipole sources collected by the objective [50]. The results of the simulations for a line of  $p^{2\omega}$  dipoles placed along a length  $L_{\text{sim}} = 720 \text{ nm}$  and  $1700 \text{ nm}$  are shown in Figs. 2(d) and 2(f). To account for the presence of a gap, we calculate the Fourier plane as a coherent beating between the far-field signals emitted from two nanowires of  $L_{\text{sim}} = 720 \text{ nm}$  and  $1700 \text{ nm}$ . The results reproduce well the experimental fringe splitting when short ( $S$ ) and long ( $L$ ) lengths contribute to the final signal with equal weights  $w_S = w_L$  [Fig. 2(e)]. We find a good match between

experimental and simulated data for values of  $L_{\text{sim}}$  in the interval  $L \pm 0.2L$ . The differences between the physical length  $L$  and  $L_{\text{sim}}$  are attributed to intrinsic oversimplification of the real electric field inherent to the OCD model and structures' defects. Among other factors is the omission of other possible mechanisms of SHG. The latter will be particularly interesting to investigate in the light of the recent discussions on ponderomotive force as well as Kerr-like and heat induced nonlinearities in metals [51,52].

To accurately fit the experimental SHG Fourier images, the coefficient  $r$  in Eq. (1) is set to 0. This implies that there is no contrapropagating field present in the cavity, which can be understood by large Ohmic losses and efficient end-face scattering [31]. Our model predicts that even if a small portion of the SP could scatter back into the cavity, a drastic change would be observed in the SHG Fourier pattern, which is not the case here. In the absence of a backreflected SP, the ODC model prediction of the scalar field  $E_{\text{SP}}^{\omega}(x)$  coincides simply with a damped wave  $e^{ik_{\text{SP}}(x+L_{\text{sim}}/2)}$ , as can be easily seen from Eq. (1). In this case, the Fourier planes are merely Fourier transforms of the  $e^{i2k_{\text{SP}}(x+L_{\text{sim}}/2)}$  function, and the observed fringes are so-called Gibbs oscillation, resulting from the finite length of the waveguide [53].

Figure 3 experimentally confirms the assumptions of delocalized nonlinear responses tested in the simulation. Figure 3(a) shows an image plane micrograph of a single rod antenna excited locally by the laser beam focused at its left extremity. The image is recorded at  $\lambda_0$ . Light scattering at the distal end unambiguously indicates the excitation of a SP mode in the antenna [44]. The corresponding spectrally filtered TPL and SHG image planes are shown in Figs. 3(b) and 3(c), respectively. Aside from the strong local spot at

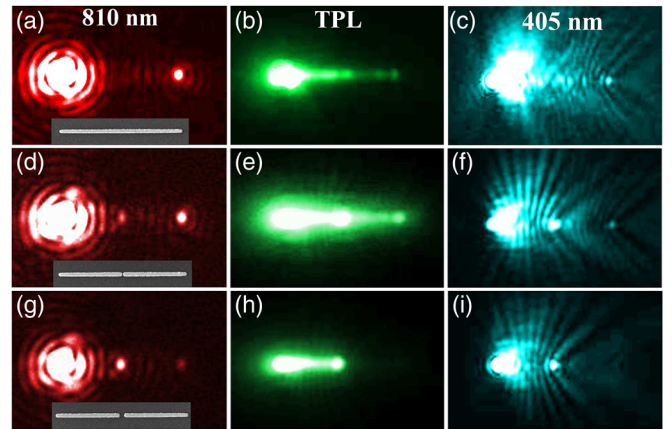


FIG. 3 (color online). (a)–(c) Colorized image plane micrographs spectrally filtered to record emission at  $\lambda_0$ , the TPL wavelength, and the SHG wavelength, respectively. The nonlinear signals are delocalized along the entire 1950-nm-long antenna. Coupled gap antennas with (d)–(f)  $g = 50 \text{ nm}$  and (g)–(i)  $180 \text{ nm}$ . Insets are SEM images of the corresponding antennas. Excitation is at the left end.

the laser position, the TPL response is delocalized along the entire rod [Fig. 3(b)]. Local scattering at the rod defects and structural discontinuities are readily observed. Similar point scattering is observed in the SHG filtered image of Fig. 3(c), together with interference patterns reminiscent of the fringes detected in Fourier planes. While these nonlinear images are somewhat degraded by residual chromatic aberrations from relay lenses, they unambiguously demonstrate that the SP mode developing in the antenna at  $\lambda_0$  carries enough energy to produce a distributed nonlinear response during its propagation. We confirm this conclusion by studying coupled gap antennas with  $g = 50$  nm and 180 nm. The images recorded at  $\lambda_0$  indicate a significant near-field coupling for the smallest gap [Fig. 3(d)]. For the decoupled rods, scattering at the gap mitigates the SP transmission to the right arm [Fig. 3(g)]. Concomitantly, the spatial extent of the nonlinear processes is gap dependent. In Figs. 3(e)–3(i), both TPL and SHG emission are observed from the second arm, in line with the fact that the SP at  $\lambda_0$  is conveyed through the gap. For decoupled antennas, the nonlinear intensity emitted along the second arm nearly vanishes due to the far-field scattering of the plasmon at the gap [Fig. 3(h)–3(i)].

Hence, the efficiency of the energy transported through the gap can be indirectly monitored by (i) observing light scattered from the gap in the linear regime [Figs. 3(d) and 3(g)] or by (ii) observing the fringe patterns in SHG Fourier planes (Fig. 2). These two aspects are brought together in Fig. 4. The coupling ratio of the SP at  $\lambda_0$  through the gap is defined as  $P_c/(P_{sc} + P_c)$ .  $P_c$  is the SP power coupled into the second arm through the gap and  $P_{sc}$  is the power scattered from the gap.  $P_c = P_{\text{end}}e^{L/2L_{SP}}$ , where  $P_{\text{end}}$  is the SP power scattered at the distal end.  $P_{sc}$  and  $P_{\text{end}}$  are directly measured from the microscope images [Figs. 3(a), 3(d), and 3(g)]. The ratio is plotted as a function of gap size in Fig. 3 (red  $\circ$ ) together with the quantity  $w_L/(w_S + w_L)$ , which describes the mixing of the two contributing antenna's dimensions. The quantities  $w_S$  and  $w_L$  are heuristically found by matching the respective experimental and theoretical Fourier planes (see the inset images). The black  $\circ$  and  $\star$  in Fig. 4 are data obtained from 1950 and 830 nm arm length, respectively. The single trend formed by all the data points supports the physical interpretation of  $w_L$  as the portion of SP power coupled into the other antenna's arm, and  $w_S$  as the portion that undergoes scattering from the gap.

From the presented theoretical model it becomes apparent that a single gold nanowire acts as a particular type of nonlinear phased array antenna. Such a device captures free propagating laser light, and frequency converts it and redirects in accordance with the modal structure of SP mediating the receiving-transmitting process. This behavior, however, can only be observed in plasmonic structure supporting substantially bound delocalized mode, as in the case of the nanowires presented in the article. Shrinking

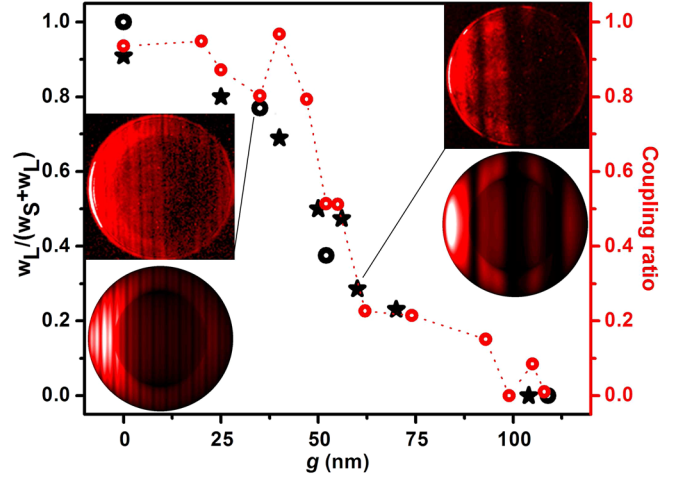


FIG. 4 (color online). Evolution of the surface plasmon coupling ratio with gaps obtained from the 1950-nm-long arm antenna (red  $\circ$ ). The data are experimentally deduced from Figs. 3(a), 3(d), and 3(g). The black  $\circ$ 's represent the mixing parameter  $w_L/(w_S + w_L)$  heuristically inferred by comparing experimental and simulated Fourier plane images. The insets are experimental and simulated Fourier planes, showing different degrees of fringe splitting for two selected gap antennas.  $\star$ 's are the mixing parameters for the set of 830-nm-long arm antennas. Comparison of coupling efficiencies in antennas of different arm lengths is justified by the fact that antennas of this size range support the similar delocalized SP mode.

their width below 100 nm results in a dominating localized response (no propagating SP excited), whereas increasing its width above 200 nm results in an increasingly leaky character of the SP mode, weaker optical near fields, and, hence, weak nonlinear response [31,32]. The absence of fringes in SHG Fourier planes marks these two other regimes (see the Supplemental Material [29]).

In summary, we demonstrate that nonlinear responses in gold rod optical antennas can have significant spatially delocalized nonlinear contributions when excited locally by a pulsed focused laser beam. This result presents an alternative—delocalized—mechanism of nonlinear excitation in plasmonic structures. As such spatially distributed responses are omnipresent in plasmonic structures, they should be considered when interpreting point-and-probe nonlinear investigations. With regards to parametric nonlinear processes, this mechanism offers new possibilities of spatial coherence control at nanoscale, for example, via plasmon-mediated (quasi-)phase matching. We anticipate that incorporation of the delocalization mechanism discussed here in today's nonlinear plasmonic discourse will incite novel ideas for tailoring of plasmonic cavities and metamaterials.

The authors acknowledge funding from FP7/20072013 Grant Agreement No. 306772 and the Agence Nationale de la Recherche (PLACORE ANR-13-BS10-0007 and Labex ACTION ANR-11-LABX-0001-01) and thank G. Bachelier for stimulating discussions.

- \*sviatlana.viarbitskaya@u-bourgogne.fr  
†alexandre.bouhelier@u-bourgogne.fr
- [1] L. Novotny and N. F. Van Hulst, *Nat. Photonics* **5**, 83 (2011).
- [2] *Optical Antennas*, edited by M. Agio and A. Alù (Cambridge University Press, Cambridge, England, 2013).
- [3] M. Kauranen and A. V. Zayats, *Nat. Photonics* **6**, 737 (2012).
- [4] H. Harutyunyan, G. Volpe, and L. Novotny, *Optical Antennas* (Cambridge University Press, Cambridge, England, 2013), p. 131.
- [5] P. Ginzburg and M. Orenstein, in *Active Plasmonics and Tuneable Plasmonic Metamaterials* (Wiley, New York, 2013), p. 41.
- [6] S. Kim, J. Jin, Y.-J. Kim, I.-Y. Park, Y. Kim, and S.-W. Kim, *Nature (London)* **453**, 757 (2008).
- [7] B. Metzger, M. Hentschel, T. Schumacher, M. Lippitz, X. Ye, C. B. Murray, B. Knabe, K. Buse, and H. Giessen, *Nano Lett.* **14**, 2867 (2014).
- [8] N. Large, M. Abb, J. Aizpurua, and O. L. Muskens, *Nano Lett.* **10**, 1741 (2010).
- [9] M. Abb, P. Albella, J. Aizpurua, and O. L. Muskens, *Nano Lett.* **11**, 2457 (2011).
- [10] G. A. Wurtz, R. Pollard, W. Hendren, G. P. Wiederrecht, D. J. Gosztola, V. A. Podolskiy, and A. V. Zayats, *Nat. Nanotechnol.* **6**, 107 (2011).
- [11] I. De Leon, J. E. Sipe, and R. W. Boyd, *Phys. Rev. A* **89**, 013855 (2014).
- [12] A. Baron, S. Larouche, D. J. Gauthier, and D. R. Smith, *J. Opt. Soc. Am. B* **32**, 9 (2015).
- [13] A. Bouhelier, R. Bachelot, G. Lerondel, S. Kostcheev, P. Royer, and G. P. Wiederrecht, *Phys. Rev. Lett.* **95**, 267405 (2005).
- [14] C. Hubert, L. Billot, P.-M. Adam, R. Bachelot, P. Royer, J. Grand, D. Gindre, K. D. Dorkenoo, and A. Fort, *Appl. Phys. Lett.* **90**, 181105 (2007).
- [15] P. Mühlischlegel, H.-J. Eisler, O. J. F. Martin, B. Hecht, and D. W. Pohl, *Science* **308**, 1607 (2005).
- [16] O. Demichel, M. Petit, G. Colas des Francs, A. Bouhelier, E. Hertz, F. Billard, F. de Fornel, and B. Cluzel, *Opt. Express* **22**, 15088 (2014).
- [17] V. Knittel, M. P. Fischer, T. de Roo, S. Mecking, A. Leitenstorfer, and D. Brida, *ACS Nano* **9**, 894 (2015).
- [18] P. Ghenuche, S. Cherukulappurath, T. H. Taminiau, N. F. van Hulst, and R. Quidant, *Phys. Rev. Lett.* **101**, 116805 (2008).
- [19] J. Berthelot, G. Bachelier, M. Song, P. Rai, G. Colas des Francs, A. Dereux, and A. Bouhelier, *Opt. Express* **20**, 10498 (2012).
- [20] V. K. Valev, B. D. Clercq, X. Zheng, D. Denkova, E. J. Osley, S. Vandendriessche, A. V. Silhanek, V. Volskiy, P. A. Warburton, G. A. E. Vandenbosch *et al.*, *Opt. Express* **20**, 256 (2012).
- [21] S. Viarbitskaya, A. Teulle, A. Cuche, J. Sharma, C. Girard, E. Dujardin, and A. Arbouet, *Appl. Phys. Lett.* **103**, 131112 (2013).
- [22] S. Viarbitskaya, A. Teulle, R. Marty, J. Sharma, C. Girard, A. Arbouet, and E. Dujardin, *Nat. Mater.* **12**, 426 (2013).
- [23] R. F. Oulton, V. J. Sorger, T. Zentgraf, R.-M. Ma, C. Gladden, L. Daia, G. Bartal, and X. Zhang, *Nature (London)* **461**, 629 (2009).
- [24] D. Saxena, S. Mokkalapati, P. Parkinson, N. Jiang, Q. Gao, H. H. Tan, and C. Jagadish, *Nat. Photonics* **7**, 963 (2013).
- [25] S. Aberra Guebrou, C. Symonds, E. Homeyer, J. C. Plenet, Y. N. Gartstein, V. M. Agranovich, and J. Bellessa, *Phys. Rev. Lett.* **108**, 066401 (2012).
- [26] G. Bachelier, I. Russier-Antoine, E. Benichou, C. Jonin, and P.-F. Brevet, *J. Opt. Soc. Am. B* **25**, 955 (2008).
- [27] F. X. Wang, F. J. Rodríguez, W. M. Albers, R. Ahorinta, J. E. Sipe, and M. Kauranen, *Phys. Rev. B* **80**, 233402 (2009).
- [28] O. Wolf, S. Campione, A. Benz, A. P. Ravikumar, S. Liu, T. S. Luk, E. A. Kadlec, E. A. Shaner, J. F. Klem, M. B. Sinclair, and I. Brener, *Nat. Commun.* **6**, 7667 (2015).
- [29] See Supplemental Material at <http://link.aps.org/supplemental/10.1103/PhysRevLett.115.197401>, including Refs. [30,31,32,33], for (I) SHG and TPL spectral and polarization content and nonlinear conversion efficiencies, (II) nonlinear delocalization vs nanowire thicknesses, (III) absence of fringes in TPL Fourier planes, and (IV) a 1D nonlinear nonlinear model.
- [30] G. T. Boyd, Z. H. Yu, and Y. R. Shen, *Phys. Rev. B* **33**, 7923 (1986).
- [31] M. Song, A. Bouhelier, P. Bramant, J. Sharma, E. Dujardin, D. Zhang, and G. Colas des Francs, *ACS Nano* **5**, 5874 (2011).
- [32] E. Verhagen, M. Spasenović, A. Polman, and L. K. Kuipers, *Phys. Rev. Lett.* **102**, 203904 (2009).
- [33] W. Ding, L. Zhou, and S. Y. Chou, *Nano Lett.* **14**, 2822 (2014).
- [34] M. Song, A. Stolz, D. Zhang, J. Arocas, L. Markey, G. Colas des Francs, E. Dujardin, and A. Bouhelier, *J. Visualized Exp.* **82**, e514048 (2013).
- [35] P. Biagioni, D. Brida, J.-S. Huang, J. Kern, L. Du, B. Hecht, M. V. Finazzi, and G. Cerullo, *Nano Lett.* **12**, 2941 (2012).
- [36] T. V. Shahbazyan, *Nano Lett.* **13**, 194 (2013).
- [37] N. Verellen, D. Denkova, B. D. Clercq, A. V. Silhanek, M. Ameloot, P. V. Dorpe, and V. V. Moshchalkov, *ACS Photonics* **2**, 410 (2015).
- [38] J.-S. Huang, J. Kern, P. Geisler, P. Weinmann, M. Kamp, A. Forchel, P. Biagioni, and B. Hecht, *Nano Lett.* **10**, 2105 (2010).
- [39] R. Czaplicki, J. Mkitalo, R. Siikonen, H. Husu, J. Lehtolahti, M. Kuittinen, and M. Kauranen, *Nano Lett.* **15**, 530 (2015).
- [40] D. de Ceglia, M. A. Vincenti, C. D. Angelis, A. Locatelli, J. W. Haus, and M. Scalora, *Opt. Express* **23**, 1715 (2015).
- [41] N. Hartmann, D. Piatkowski, R. Ciesielski, S. Mackowski, and A. Hartschuh, *ACS Nano* **7**, 10257 (2013).
- [42] T. Shegai, V. D. Miljković, K. Bao, H. Xu, P. Nordlander, P. Johansson, and M. Käll, *Nano Lett.* **11**, 706 (2011).
- [43] I. Sersic, C. Tuambilangana, and A. F. Koenderink, *New J. Phys.* **13**, 083019 (2011).
- [44] R. M. Dickson and L. A. Lyon, *J. Phys. Chem. B* **104**, 6095 (2000).
- [45] H. Wei and H. Xu, *Nanophotonics* **1**, 155 (2012).
- [46] T. H. Taminiau, F. D. Stefani, and N. F. van Hulst, *Nano Lett.* **11**, 1020 (2011).
- [47] The finite element simulations were performed using a mode solver based on finite element method (COMSOL Multiphysics, RF Module). The dielectric constant of gold is taken from tabulated data [P. B. Johnson and R. W. Christy, *Phys. Rev. B* **6**, 4370 (1972)].

- [48] J. Dorfmueller, R. Vogelgesang, R. Weitz, C. Rockstuhl, C. Etrich, T. Pertsch, F. Lederer, and K. Kern, *Nano Lett.* **9**, 2372 (2009).
- [49] K. Thyagarajan, S. Rivier, A. Lovera, and O. J. Martin, *Opt. Express* **20**, 12860 (2012).
- [50] L. Novotny and B. Hecht, *Principles of Nano-Optics*, 2nd ed. (Cambridge University Press, Cambridge, England, 2012), p. 543; calculations were implemented using Matlab.
- [51] P. Ginzburg, A. V. Krasavin, G. A. Wurtz, and A. V. Zayats, *ACS Photonics* **2**, 8 (2015).
- [52] A. Marini, M. Conforti, G. D. Valle, H. W. Lee, T. X. Tran, W. Chang, M. A. Schmidt, S. Longhi, P. S. J. Russell, and F. Biancalana, *New J. Phys.* **15**, 013033 (2013).
- [53] K. Hassan, A. Bouhelier, T. Bernardin, G. Colas-des-Francis, J.-C. Weeber, A. Dereux, and R. Espiau de Lamaestre, *Phys. Rev. B* **87**, 195428 (2013).